

# Microstructure and optical properties of Au–Y<sub>2</sub>O<sub>3</sub>-stabilized ZrO<sub>2</sub> nanocomposite films

George Sirinakis, Rezina Siddique, Christos Monokroussos,<sup>a)</sup> Michael A. Carpenter,<sup>b)</sup> and Alain E. Kaloyeros

*College of Nanoscale Science and Engineering, The University at Albany—State University of New York, Albany, New York 12203*

(Received 9 February 2005; accepted 31 May 2005)

Nanocomposite films consisting of gold nanoparticles embedded in an yttria stabilized zirconia (YSZ) matrix were synthesized at room temperature by radio-frequency co-sputtering from YSZ and Au targets at a 5 mTorr working pressure. The films were subsequently annealed for 2 h in 1 atm argon, with the annealing temperature varied from 600 to 1000 °C in steps of 100 °C. The composition, microstructure, and optical properties of the films were characterized as a function of annealing temperature by Rutherford backscattering spectrometry, scanning electron microscopy, Auger electron spectroscopy, x-ray diffraction, and absorption spectroscopy. An optical absorption band due to the surface plasmon resonance (SPR) of the Au nanoparticles was observed around a wavelength of 600 nm. Furthermore, the SPR band full width at half-maximum exhibited an inverse linear dependence on the radius of the Au nanoparticle, with a slope parameter  $A = 0.18$ , indicating a weak interaction between the YSZ matrix and the Au nanoparticles. The experimentally observed SPR dependence on nanoparticle size is discussed within the context of the Mie theory and its size-dependent optical constants.

## I. INTRODUCTION

Nanosized metal particles embedded in various oxide matrices are currently of significant interest because they exhibit customizable optical, electronic, and magnetic properties that could be utilized in a myriad of novel technologies, including optoelectronic devices, portable sensors, and high-density information storage applications.<sup>1,2</sup> In particular, silver (Ag) and gold (Au) nanoparticles exhibit a strong surface plasmon resonance (SPR) band, whose spectral position and shape are not only highly dependent on the size, shape, and density of the nanoparticles, but also on the structural and chemical characteristics of the host medium.<sup>2</sup>

Although it has been demonstrated that noble metal nanoparticles exhibit significant potential in optical sensing devices,<sup>3</sup> embedding the nanoparticles in an appropriate matrix is believed to broaden their operational range, thus permitting a new and expanded array of technological applications.<sup>4</sup> In this context, a vast majority of

the investigations to date of the optical properties of embedded Au nanoparticles has concentrated on studying the optical properties of Au in amorphous binary oxide matrices, including silicon oxide (SiO<sub>2</sub>) and aluminum oxide (Al<sub>2</sub>O<sub>3</sub>). Although these matrices are generally considered inert, evidence indicates that the material and microstructural properties of the matrix may cause unexpected changes in the SPR peak position dependence on the nanoparticle diameter. More specifically, while it is widely accepted that the SPR band of free spherical Ag or Au nanoparticles will red shift with an increase in particle diameter, Au nanoparticles embedded in seemingly inert amorphous matrices exhibit an SPR band, which could either red shift or blue shift with an increase in the average nanoparticle diameter.<sup>5–7</sup>

In this respect, research by the current investigators has focused on extending the scientific progress achieved to the characterization of the optical properties of Au nanoparticles in a polycrystalline yttria (Y<sub>2</sub>O<sub>3</sub>) stabilized zirconia (ZrO<sub>2</sub>) matrix. The primary motivation is to perform the baseline studies required for the future development of all-optical chemical sensors that use noble metal nanoparticles in crystalline ternary and quaternary oxide matrices. The latter would enable applications under more aggressive chemical, thermal, and environmental conditions than previously possible. Accordingly, the present article is the first in a series of reports from a

<sup>a)</sup>Present address: Centre for Renewable Energy Systems Technology, Department of Electronic and Electrical Engineering, Loughborough University, Loughborough, LE11 3TU, UK.

<sup>b)</sup>Address all correspondence to this author.

e-mail: mcarpenter@uamail.albany.edu

DOI: 10.1557/JMR.2005.0300

demonstration of feasibility study that investigated the appropriateness of YSZ as the host medium for Au nanoclusters.

Yttria-stabilized zirconia (YSZ) is a refractory material with excellent thermal, chemical, and mechanical properties. It has been proved suitable for optical applications due to its high refractive index, low absorption coefficient, and high transparency in the visible and infrared regions.<sup>8</sup> The material has also witnessed a wide range of other applications, including in thermal barrier layers, corrosion resistant coatings,<sup>9</sup> and solid oxide fuel cells (SOFC), both as an electrolyte and a cathode (when doped with nickel).<sup>10</sup> Thus, its use as a base platform in nanocomposite thin films is projected to provide significant benefits for applications in high-temperature sensor technologies, especially since the resulting system could be integrated directly into SOFC systems. In this context, it is widely accepted that optical sensing is inherently safer and more reliable than its electrical counterpart.

The current article reports on the composition, microstructure, and optical properties of Au nanoparticles embedded in a YSZ matrix. In particular, results are presented on the microstructure and optical properties of the nanocomposite films as a function of post-deposition annealing temperature in the 300–800 nm wavelength spectral region. The dependence of the SPR band on particle size is discussed within the context of Mie theory and the size-dependent dielectric functions.<sup>11</sup>

## II. EXPERIMENTAL CONDITIONS

Depositions were carried out in a high-vacuum capable, custom-designed sputtering system. The system consisted of a stainless steel chamber equipped with two confocally designed “MAK” type magnetron sputtering guns, manufactured by US Incorporated, mounted on individually retractable vacuum compatible mechanical feedthroughs. Each sputtering source was driven by a 13.56 MHz radio-frequency (rf) power supply model number AE RFX600, manufactured by Advanced Energy. The YSZ and Au targets were, respectively, a 5.08-cm-diameter disk of ZrO<sub>2</sub> stabilized with 5 wt% Y<sub>2</sub>O<sub>3</sub> (99.9% purity), and a 5.08-cm-diameter disk of Au (99.99% purity), both fabricated by Williams Advanced Materials. The sputtering chamber was equipped with a shutter system that enabled complete isolation of the targets from the substrates during the initial stages of plasma formation and pre-deposition target clean-up.

Two types of substrates were used: single crystal (100) silicon (Si) and optical-quality sapphire provided by Edmund Industrial Optics. In a typical deposition run, the silicon substrates were first ultrasonically cleaned prior to loading in the chamber for 5 min in ethanol and then in acetone to remove excess surface organic material, while the sapphire substrates were used as received. The

substrates were then loaded in the sputtering chamber, and the latter was pumped down to a base pressure of  $\sim 5 \times 10^{-7}$  Torr using a turbomolecular pump.

The distance between the substrate and the YSZ and Au targets were set at 50 and 85 mm, respectively. Argon (99.999% purity) gas flow was then initiated at 5 sccm and co-sputtering was realized at an operating pressure of  $5 \times 10^{-3}$  Torr. Pre-deposition target clean up was performed by sputtering with the shutters closed for 60 min at 200 W rf power for the YSZ target and for 15 min at 20 W rf power for the Au target. Depositions were performed for 15 min at 200 and 20 W rf power for the YSZ and Au target, respectively. The as-deposited films were subsequently annealed ex situ at 600, 700, 800, 900, and 1000 °C for 2 h in an Ar atmosphere. Typical sputtering and annealing conditions are summarized in Table I. The silicon substrates were used for thickness measurements and auger electron spectroscopy (AES) analysis, while the sapphire substrates were utilized to determine the optical properties and the microstructure of the resulting nanocomposite films.

## III. CHARACTERIZATION TECHNIQUES

The microstructure of the as-deposited and post-annealed Au-YSZ nanocomposite films was examined by x-ray diffraction (XRD). The XRD patterns were derived on a Scintag XDS 2000 x-ray diffractometer using Cu K<sub>α</sub> radiation. The XRD system was equipped with a horizontal wide angle four-axis goniometer with stepping motors, which allowed independent or coupled  $\theta/2\theta$  axes motion. XRD spectra were collected in the standard  $\theta$ -2 $\theta$  mode with  $2\theta$  ranging from 25° to 55° in steps of 0.03°. The collected XRD patterns were compared to the Cu reference patterns from the standard Joint Committee for Powder Diffraction Standards (JCPDS) powder diffraction files, PDF No. 802187 for YSZ and PDF No. 040784 for Au, for crystalline phase identification. The average crystallite size  $D$  was calculated from the Scherrer formula<sup>12</sup>

$$D = \frac{0.9\lambda}{B \cos \theta} ,$$

where  $\lambda$  is the x-ray wavelength,  $B$  is the full width at half-maximum (FWHM) of the appropriate elemental XRD peak and  $\theta$  is the diffraction angle. The elemental XRD peak was fit using a Lorentzian curve.<sup>13</sup> (A

TABLE I. Typical sputtering and post-deposition annealing parameters.

Sputtering parameters	Annealing parameters
Process pressure: 5 mTorr	Atmosphere: Ar at 760 Torr
rf power (YSZ): 200 W	Temperature: 600, 700, 800,
rf power (Au): 20 W	900, 1000 °C
YSZ target-substrate distance: 50 mm	Time: 2 h
Au target-substrate distance: 85 mm	

Lorentzian peak is more appropriate than a Gaussian profile when the broadening of the XRD peak is due to nanograins instead of stress or strain.)

Optical absorption spectra were measured under ambient laboratory conditions using a Hewlett Packard 8452A diode array spectrophotometer in the wavelength region from 300 to 800 nm with a step size of 2 nm. For accurate background subtraction, the absorption spectrum of an as-received sapphire substrate was measured prior to each nanocomposite sample. Films with thicknesses of approximately 100 nm were used. A LEO 1550 scanning electron microscope (SEM) operated at a 5 keV primary electron beam was used for film thickness measurements.

The Au content was found to be approximately 10 at.% measured using a Perkin-Elmer PHI 600 Auger Electron Spectroscopy (AES) system employing a cylindrical mirror analyzer. The primary electron beam energy was 10 keV, at 1  $\mu$ A, yielding a spot size of approximately 1  $\mu$ m. Relative compositional depth uniformity of the deposited Au-YSZ films can be determined within 10% relative experimental accuracy. Finally, the spatial distribution of Au atoms as a function of film depth was measured by Rutherford backscattering spectroscopy (RBS) on a Dynamitron linear accelerator using a 3.0 MeV <sup>4</sup>He<sup>+</sup> primary ion beam.

## IV. RESULTS AND DISCUSSION

### A. Film microstructure and morphology as a function of annealing temperature

Figure 1 displays typical XRD patterns for the evolution of the microstructure of Au-YSZ nanocomposite

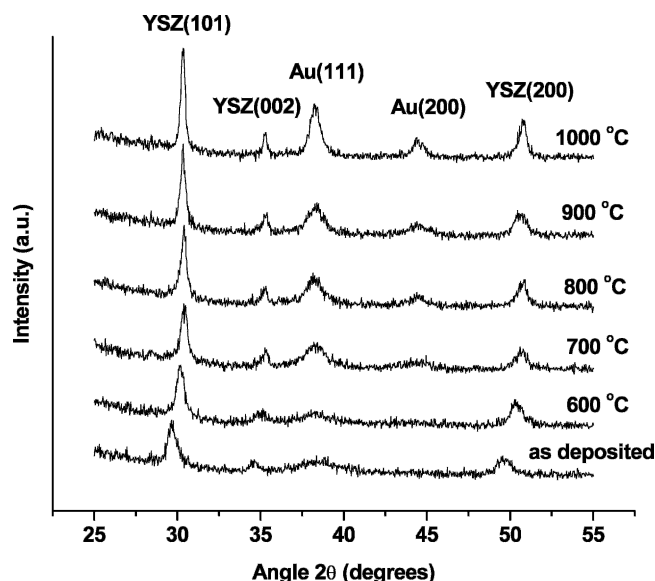


FIG. 1. X-ray diffraction patterns of Au-YSZ nanocomposite films as a function of annealing temperature.

films as a function of annealing temperature. The XRD patterns are plotted as diffraction peak intensity versus diffraction angle  $2\theta$  for the range from 25° to 55°. As can be seen in Fig. 1, two polycrystalline phases were detected, one corresponding to the tetragonal YSZ phase, and the other to the face centered cubic Au phase. In addition, the XRD peaks became sharper and more intense with higher annealing temperature, indicating an increase in the crystallinity, and hence a rise in the average size of both the YSZ and the Au crystallites. These trends are expected and are attributed to the availability of a larger thermal energy at higher annealing temperature to drive crystallite coalescence, growth, and realignment.

The average Au crystallite size was calculated from the Scherrer formula<sup>12</sup> using the Au XRD (111) reflection. The results of this analysis are displayed in Fig. 2, which plots the average crystallite size for Au as a function of annealing temperature. Figure 2 indicates that the average Au crystallite size exhibited a gradual rise with annealing temperature, from  $\sim$ 4.0 nm at 600 °C to  $\sim$ 8.0 nm at 800 °C to  $\sim$ 9.5 nm at 900 °C. However, a marked increase of  $\sim$ 5.5 nm was observed as the annealing temperature was increased from 900 to 1000 °C, indicating a potential change in the underlying mechanism that drives the coalescence and regrowth of the Au crystallites.

Figure 3 displays RBS data for the spatial distribution of Au atoms versus film depth within the YSZ matrix. The data are plotted as elemental RBS peak intensity versus RBS channel, with the width and the height of each peak determined by the spatial distribution and relative concentration of the corresponding element,

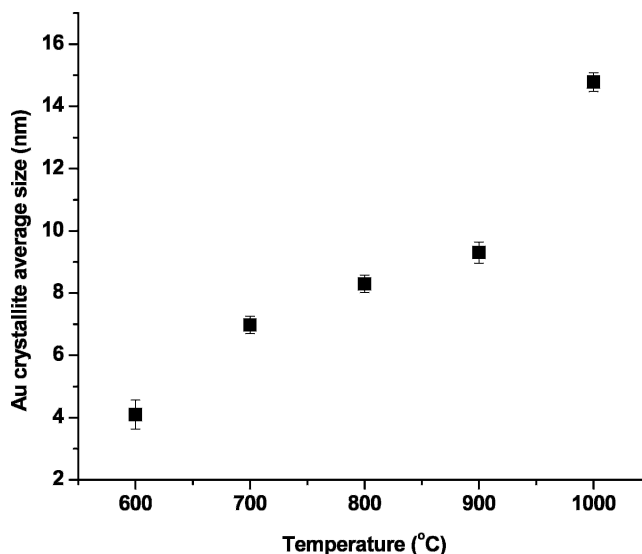


FIG. 2. Average Au crystallite size versus annealing temperature. The error bars were estimated by an error propagation analysis from the errors in the FWHM and the peak position resulting from a Lorentzian fit to the Au (111) XRD reflection.

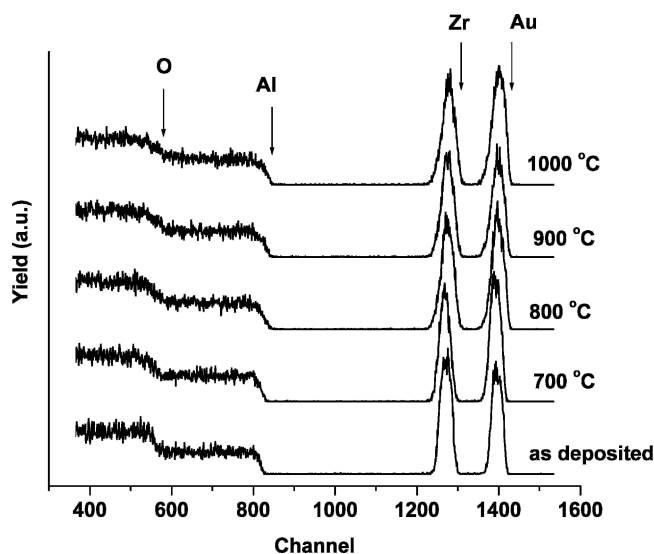


FIG. 3. RBS spectra of Au-YSZ nanocomposite films as a function of annealing temperature.

respectively. In this context, no significant change was observed in the height or FWHM of the Au RBS peak with respect to the Zr peak as a function of annealing temperature, indicating that the average concentration of Au atoms as a function of film depth is not affected by the annealing process.

These findings, when coupled to the increase reported above in the average Au crystallite size with the rise in annealing temperature, imply that at temperatures below 900 °C, Au crystallites grow through a solid state diffusion mechanism of individual Au atoms through the YSZ matrix. Alternatively, above 900 °C, the annealing temperature approaches the melting point of Au. The latter is 1064 °C for bulk Au<sup>14</sup> but has been shown to be significantly lower for Au in nanoparticle form.<sup>15</sup> For instance, a melting point of 900 °C was reported for 10-nm silica-encapsulated Au particle.<sup>16</sup>

Accordingly, it is believed that above 900 °C, the growth of Au crystallites is still governed by the diffusion of Au atoms through the YSZ matrix. However, in contrast to solid-state diffusion of individual Au atoms observed below 900 °C, the marked increase in Au crystallite size above 900 °C suggests the occurrence of Au crystallite growth via an Ostwald ripening process. In this process, larger Au crystallites with lower interfacial curvature grow at the expense of their smaller counterparts with higher interfacial curvature, via the migration of individual Au atoms.<sup>17</sup> This suggestion is in agreement with previous studies on the growth mechanism of Au nanoparticles in a silica matrix.<sup>5</sup>

## B. Film optical properties as a function of annealing temperature

Figure 4 shows typical absorbance spectra of Au-YSZ nanocomposite films over the wavelength region from

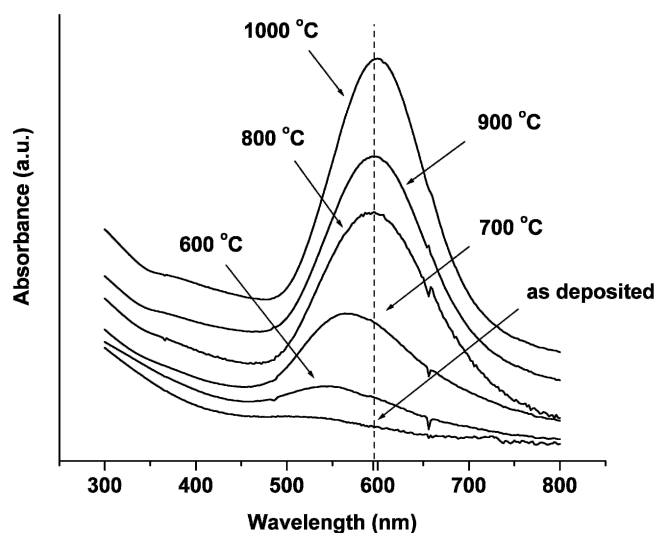


FIG. 4. Absorption spectra of Au-YSZ nanocomposite films as a function of annealing temperature. The dashed vertical line indicates the position of the SPR band as predicted from the Mie theory using bulk dielectric functions for Au and for YSZ as measured by spectroscopic ellipsometry.

300 to 800 nm. As can be seen in Fig. 4, a SPR band due to the light-induced collective, oscillatory motion of the conduction electrons of Au is prominently present around 600 nm. The band maximum was observed to shift toward longer wavelengths and become sharper and more intense with higher annealing temperature. The corresponding FWHM was calculated by doubling the value of the half width at half-maximum (HWHM), with the latter being derived from the area under the absorbance intensity curve extending from the absorbance band maximum towards longer wavelengths. This approach was necessitated by the fact that the Au *5d*-*6sp* interband transitions, with an onset energy around 2.4 eV (517 nm), affect the shape of the absorption peak on the low wavelength side, resulting in an asymmetric peak profile.<sup>18</sup>

In addition, Fig. 5 plots the FWHM of the Au-YSZ SPR band versus the inverse of the nanoparticle radius as determined from XRD analysis. It is observed that the FWHM increases linearly as a function of the inverse of the nanoparticle radius. This experimentally observed SPR dependence on nanoparticle size is discussed below within the context of the Mie theory and its size-dependent optical constants, given that it provides a straightforward and effective tool to describe the optical properties of metal nanoparticles.<sup>11</sup>

In the Mie treatment, the interaction of electromagnetic radiation with a physical system, approximated as a sphere whose size is much smaller than the wavelength of the incident light, is treated using Maxwell's equations. In this treatment, the optical properties of the system are introduced through appropriately chosen dielectric functions. This approach is particularly appropriate

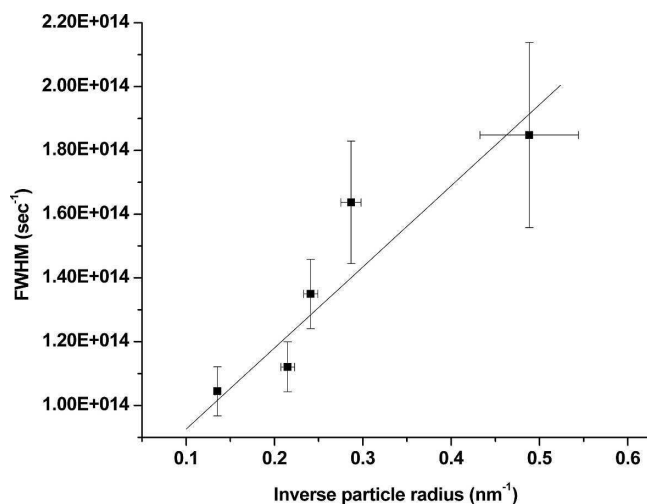


FIG. 5. FWHM of the surface plasmon resonance absorption band of Au-YSZ nanocomposite films versus inverse particle radius.

for the case of small particles in which the bulk dielectric functions are expected to have limited applicability, due either to structural changes or finite size effects, such as a reduced mean free path for electron scattering.

In particular, for nanoparticles with sizes smaller than or comparable to the bulk mean free path of the conduction electron, collisions of the conduction electron with the surface of the particle become increasingly important and result in an effective mean free path which is smaller than the bulk value. For spherical particles, this reduced mean free path effect can be described by a modified Drude damping constant<sup>19</sup>

$$\gamma(R) = \gamma_b + A \frac{v_F}{R}, \quad (1)$$

where  $\gamma_b$  is the damping constant of the bulk conduction electrons,  $v_F$  is the Fermi velocity,  $R$  is the particle radius, and  $A$  is a coefficient that depends on the characteristics of the metal nanoparticle/host matrix.

The coefficient  $A$  plays a key role in elucidating the underlying optical sensing mechanism that guides the nanocomposite system. In particular, the magnitude of  $A$  is directly proportional to the degree of interaction between the metal nanoparticles and the embedding medium, and can thus provide critical information on the nature of the metal-matrix interface.<sup>20,21</sup> For example, a higher  $A$  value was reported for Ag nanoclusters within a SiO<sub>2</sub> matrix, as compared to free Ag clusters. The higher  $A$  value was indicative of the availability of additional channels for dissipation of plasmon energy within the SiO<sub>2</sub> matrix.<sup>19</sup>

The value of  $A$  is determined experimentally from the slope of the plot of the FWHM of the SPR band versus nanoparticle size, as shown in Fig. 5. The data in Fig. 5 can be fit reasonably well using a linear regression, which yields values for  $\gamma_b$  and  $A$  of, respectively,  $6.7 \times$

$10^{13} \text{ s}^{-1}$  and 0.18. The experimentally derived value for  $\gamma_b$  is within a factor of two of the theoretical prediction for bulk Au ( $3.3 \times 10^{13} \text{ s}^{-1}$ ),<sup>22</sup> thus indicating that the Au-YSZ system follows the  $1/R$  dependence of the SPR bandwidth. Alternatively, a quantitative comparison of the experimental value of  $A$  cannot be made with theoretical predictions, since it would require detailed knowledge of the physical and chemical nature of the Au-YSZ interface. However, the experimental value of 0.18 indicates a weak interaction between the Au nanoparticles and the YSZ matrix. This finding is further supported by x-ray photoelectron spectroscopy (XPS) studies of ultrathin Au layers on YSZ (100) substrates,<sup>23,24</sup> which indicated the absence of any electron transfer and, accordingly, a weak interaction between Au and YSZ.

Figure 6 displays the peak position of the SPR band as a function of particle size. As the particle size is increased from  $\sim 4$  to  $\sim 8$  nm, there is a marked red-shift in the position of the peak from, respectively,  $\sim 550$  nm up to  $\sim 595$  nm. Upon further increase of the particle size to  $\sim 15$  nm, the peak experiences a slight red-shift leveling off at  $\sim 600$  nm. Furthermore, the observed SPR band shift as a function of annealing temperature is not dependent on changes in the YSZ matrix, as the optical properties of the matrix were studied extensively by means of spectroscopic ellipsometry and the refractive index of the YSZ matrix was found to be unaffected by the annealing temperature.

A comparison to previous experimental work on nanocomposite films with embedded Au and Ag nanoparticles is possible for amorphous matrices like SiO<sub>2</sub> or Al<sub>2</sub>O<sub>3</sub>. While these matrices are generally considered inert, it is apparent that their specific material and

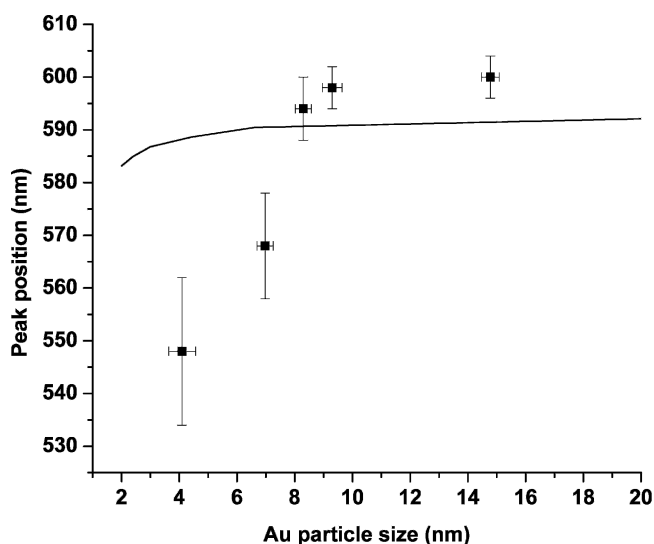


FIG. 6. Peak position of the surface plasmon resonance absorption band of Au-YSZ nanocomposite films as a function of the annealing temperature. The solid line corresponds to the prediction of the core-shell model using  $\alpha = 0.1$  nm.

microstructural properties affect the SPR peak dependence on particle size, resulting in opposing shifts of the SPR band even for the same matrix. More specifically, Fukumi et al.<sup>5</sup> observed a redshift of the SPR band for Au nanoparticles implanted in a silica glass matrix with an increase in particle size. Tanahashi et al.<sup>6</sup> reported a blueshift of the SPR band of Au nanoparticles embedded in a SiO<sub>2</sub> matrix with an increase in particle size, and Hosoya et al.<sup>7</sup> observed a pronounced blueshift of the SPR band of embedded Au particles in Al<sub>2</sub>O<sub>3</sub> with an increase in particle size.

A redshift of the SPR band with an increase in particle size is an expected result that has been observed for free spherical Ag nanoparticles.<sup>19</sup> This behavior can be understood in terms of the different spatial distribution of the *s*- and the *d*-wave functions with the latter being more localized.<sup>25</sup> Therefore, part of the *s* electron density is not screened by the *d* electron density and oscillates with the unscreened plasma frequency, i.e., the Drude plasmon frequency, resulting in a redshift of the SPR band with increasing particle size.

Similar behavior is expected for free spherical Au nanoparticles since the spatial distribution of the *d*- and *s*-wave functions are comparable to those for Ag.<sup>26</sup> However, in the case where there are available electronic states in a surrounding medium with energies nearly overlapping the occupied states of the nanoparticle, such as dangling bonds in the case of non-inert amorphous matrices, electrons can be transferred from the particle to the matrix. This results in a reduced free electron density and a corresponding blueshift of the SPR band with increasing particle size.<sup>7</sup> Therefore, it can be argued that crystalline matrices like YSZ offer a more inert environment than amorphous matrices for the nanoparticles due to the presence of a reduced density of dangling bonds. The resulting material system could thus behave in a more expected and reliable way, in contrast to the variable shifts observed in the case of amorphous matrices.

A core-shell model is used here to describe the shift of the SPR band of the Au-YSZ system as a function of particle size. The model has been proven to provide reasonable agreement with experimental data for embedded Ag<sup>27</sup> and Au<sup>7</sup> nanoparticles in, respectively, rare-gas and amorphous alumina matrices. In this model, the core is described by the bulk Au dielectric function ( $\epsilon_{\text{Au}}$ )<sup>28</sup> and the shell is described by the Drude free electron dielectric function ( $\epsilon_{\text{Drude}}$ ). In this case, the extinction cross section ( $\sigma$ ) can be derived as function of the particle volume *V*, the speed of light *c*, dielectric function of the YSZ matrix  $\epsilon_{\text{YSZ}}$ , and the thickness of the shell where the *d*-electron screening is ineffective (0.1 nm for Au).<sup>26</sup> Transfer of electrons from the particle to the matrix is disregarded on the basis of the weak interaction between the Au nanoparticle and the YSZ matrix. The predictions of the model for the peak position of the SPR band as a function

of Au nanoparticle size are shown in Fig. 6 (solid line). Although the model is successful in qualitatively describing the redshift of the SPR band with increasing particle size, the shifts of the SPR band are significantly underestimated.

The above discussion indicates that the marked shift in the Au-YSZ SPR band for samples annealed up to 800 °C cannot be explained strictly within the context of the core-shell model. Additional effects on the dielectric function of Au related to Au nanoparticle structural phase transition from nanocluster form to the bulk state should also be taken into account. Recent work suggested that the critical size for this transition is around 10 nm.<sup>29</sup> This value is in good agreement with the XRD data reported by the present investigators in Fig. 2. As seen in the figure, the Au grain size exhibited a gradual rise with annealing temperature, from ~4.0 nm at 600 °C to ~8.0 nm at 800 °C, with the nanoparticle growth occurring through a solid state diffusion mechanism of individual Au atoms through the YSZ matrix.

## V. CONCLUSIONS

Au-YSZ nanocomposite films were synthesized by rf magnetron co-sputtering followed by post-deposition annealing. It was found that the degree of crystallinity of the YSZ matrix and average Au nanoparticle size increased with higher annealing temperature. The latter was attributed to diffusion of Au atoms through the YSZ matrix. An absorption band attributed to the surface plasmon resonance of the Au nanoparticles was observed at ~600 nm. The peak of the SPR band red-shifted and the FWHM decreased with increasing annealing temperatures. The red-shift of the SPR band was attributed to a structural phase transition from cluster to a bulk state for Au nanoparticles. The transition occurred at a nanocluster size of ~8 nm, in excellent agreement with prior work in the literature. Furthermore, it was found that the Au-YSZ system follows the 1/*R* dependence of the FWHM of the SPR band with a slope parameter *A* = 0.18, indicating a weak interaction between the YSZ matrix and the Au nanoparticles. As such, the Au-YSZ nanocomposite system behaves in a similar manner as free Au nanoparticles.

## ACKNOWLEDGMENTS

This work was supported by the United States Department of Energy National Energy Technology Laboratory under Contract Nos. DE-FG26-02NT41542 and DE-FG26-04NT42184, and the New York State Office of Science, Technology and Academic Research (NYSTAR). This support is gratefully acknowledged. Any opinions, findings, and conclusions or recommendations expressed in this publication are those of the

authors and do not necessarily reflect the views of the United States Department of Energy National Energy Technology Laboratory.

## REFERENCES

1. C.B. Murray, C.R. Keglar, and M.G. Bawendi: Synthesis and characterization of monodisperse nanocrystals and close-packed nanocrystal assemblies. *Annu. Rev. Mater. Sci.* **30**, 545 (2000).
2. S. Link and M.A. El-Sayed: Optical properties and ultrafast dynamics of metallic nanocrystals. *Annu. Rev. Phys. Chem.* **54**, 331 (2003).
3. A.D. MacFarland and R.P. Van Duyne: Single silver nanoparticles as real-time optical sensors with zeptomole sensitivity. *Nano Lett.* **3**, 1057 (2003).
4. M. Ando, T. Kobayashi, S. Iijima, and M. Haruta: Optical CO sensitivity of Au–CuO composite film by use of the plasmon absorption change. *Sens. Actuators B* **96**, 589 (2003).
5. K. Fukumi, A. Chayahara, K. Kadono, T. Sakaguchi, Y. Horino, M. Miya, K. Fujii, J. Hayakawa, and M. Satou: Gold nanoparticles ion implanted in glass with enhanced nonlinear optical properties. *J. Appl. Phys.* **75**, 3075 (1994).
6. I. Tanahashi, Y. Manabe, T. Tohda, S. Sasaki, and A. Nakamura: Optical nonlinearities of Au/SiO<sub>2</sub> composite thin films prepared by a sputtering method. *J. Appl. Phys.* **79**, 1244 (1996).
7. Y. Hosoya, T. Suga, T. Yanagawa, and Y. Kurokawa: Linear and nonlinear optical properties of sol-gel-derived Au nanometer-particle-doped alumina. *J. Appl. Phys.* **81**, 1475 (1997).
8. M. Boulouze, A. Boulouze, A. Giani, and A. Boyer: Influence of substrate temperature and target composition on the properties of yttria-stabilized zirconia thin films grown by r.f. reactive magnetron sputtering. *Thin Solid Films* **323**, 85 (1998).
9. G. Johner and J.K. Schweitzer: Thermal-barrier coatings for jet engine improvement. *Thin Solid Films* **119**, 301 (1984).
10. S.C. Singhal: Advances in solid oxide fuel cell technology. *Solid State Ionics* **135**, 305 (2000).
11. C.F. Bohren and D.R. Huffman: *Absorption and Scattering of Light by Small Particles* (Wiley, New York, 1983), p. 82.
12. B.D. Cullity and S.R. Stock: *Elements of X-ray Diffraction*, 3rd ed. (Prentice-Hall, Upper Saddle River, NJ, 2001), p. 388.
13. A.R.L. Thermo (private communication, 2003).
14. D.R. Lide: *Handbook of Chemistry and Physics*, 83rd ed. (CRC Press LLC, Boca Raton, FL, 2002).
15. G.L. Allen, R.A. Bayles, W.W. Gile, and W.A. Jesser: Small particle melting of pure metals. *Thin Solid Films* **144**, 297 (1986).
16. K. Dick, T. Dhanasekaran, Z. Zhang, and D. Meisel: Size-dependent melting of silica-encapsulated gold nanoparticles. *J. Am. Chem. Soc.* **124**, 2312 (2002).
17. G. De Marchi, G. Mattei, P. Mazzoldi, C. Sada, and A. Miotello: Two stages in the kinetics of gold cluster growth in ion-implanted silica during isothermal annealing in oxidizing atmosphere. *J. Appl. Phys.* **92**, 4249 (2002).
18. N.E. Christensen and B.O. Seraphin: Relativistic band calculation and the optical properties of gold. *Phys. Rev. B* **4**, 3321 (1971).
19. H. Hövel, S. Fritz, A. Hilger, U. Kreibig, and M. Vollmer: Width of cluster plasmon resonances: Bulk dielectric functions and chemical interface damping. *Phys. Rev. B* **48**, 18178 (1993).
20. B.N.J. Persson: Polarizability of small spherical metal particles: Influence of the matrix environment. *Surf. Sci.* **281**, 153 (1993).
21. U. Kreibig and M. Vollmer: *Optical Properties of Metal Clusters* (Springer, New York, 1995).
22. N.W. Ashcroft and N.D. Mermin: *Solid State Physics* (Saunders College Publishing, New York, NY, 1976), pp.10.
23. S. Zafeiratos and S. Kennou: A study of gold ultrathin film growth on yttria-stabilized ZrO<sub>2</sub>(100). *Surf. Sci.* **443**, 238 (1999).
24. S. Zafeiratos, S. Neophytides, and S. Kennou: A photoelectron spectroscopy study of Au thin films on ZrO<sub>2</sub> (100). *Thin Solid Films* **386**, 53 (2001).
25. V. Kresin: Collective resonances in silver clusters: Role of d electrons and the polarization-free surface layer. *Phys. Rev. B* **51**, 1844 (1995).
26. B. Palpant, B. Prével, J. Lermé, E. Cottancin, M. Pellarin, M. Treilleux, A. Perez, J.L. Vialle, and M. Broyer: Optical properties of gold clusters in the size range 2–4 nm. *Phys. Rev. B* **57**, 1963 (1998).
27. S. Ferdigo, W. Harbich, and J. Buttet: Collective dipole oscillations in small silver clusters embedded in rare-gas matrices. *Phys. Rev. B* **47**, 10706 (1993).
28. P.B. Johnson and R.W. Christy: Optical constants of the noble metals. *Phys. Rev. B* **6**, 4370 (1972).
29. D. Dalacu and L. Martinu: Spectroellipsometric characterization of plasma-deposited Au/SiO<sub>2</sub> nanocomposite films. *J. Appl. Phys.* **87**, 228 (2000).